Dimensional characteristics and mechanical properties of

laser-formed parts

Wenchuan Li, Jiangcheng Bao, and Y. Lawrence Yao*

Department of Mechanical Engineering
Columbia University
New York, NY 10027

* Corresponding author.

Abstract

Recent developments in the study of the laser bending process are reviewed and presented to obtain new perspectives along the lines of dimensional characteristics and mechanical properties of the formed parts. Both numerical and experimental results are described and compared. The dimensional characteristics examined include bending angle variation and bending edge curving. The mechanical properties examined include residual stress, hardness and microstructural change.

1. Introduction

Laser forming process has its roots in the traditional flame bending, where the sheet metal is heated and deformed by an oxy-acetylene torch. Laser forming is a process in which metal workpiece is heated along a certain path with a defocused laser beam, and with or without cooling of a jet stream of gas or water emulsion, so that laser-induced thermal expansion and contraction result in deformation of the metal, without a hard forming tool or external forces. It is therefore a flexible forming technique suitable for low-volume production and/or rapid prototyping of sheet metal, as well as for adjusting

and aligning sheet metal components (Magee, et al., 1998). It has potential applications in aerospace, shipbuilding, microelectronics and automotive industries.

Understanding various aspects of the laser forming is a challenging problem of considerable theoretical and practical interest. Experimental and theoretical investigations have been reported to understand the mechanisms involved in the laser forming. The proposed mechanisms are temperature gradient mechanism (TGM) (Vollertsen, 1994a), buckling mechanism (BM) (Arnet and Vollertsen, 1995), and upsetting mechanism depending on operation conditions, material properties and workpiece thickness. A number of analytical models were derived to predict the bending angle α (Fig.1) in the straight-line laser bending (Vollertsen, 1994). Some of the models are in reasonable agreement with experimental results. Numerical investigations were conducted using the finite element method. Alberti, et al. (1994) carried out a numerical simulation of the laser bending process by a coupled thermal mechanical analysis. Temperature dependency of flow stress was taken into consideration. Hsiao, et al. (1997) simulated the bending process by taking into account convection and radiation at boundaries, and using extrapolation for mechanical properties at higher temperature. Holzer, et al. (1994) modeled the bending process under the BM. As temperature often rises fairly high in laser forming, taking into account temperature dependency of material properties becomes important to the simulation accuracy. Large deformation is desired in laser forming, and consequently, it is necessary to consider strain hardening, especially in the case of multiple scan (Sprenger, et al., 1994).

Despite of the progress made to date, there still exist problems that need to be addressed before laser forming becomes a practical processing technology. Among them are the thorough understandings of the major effects that influence the dimensional characteristics and mechanical properties of laser formed components. For instance, edge effect that is characterized by variation of the bending angle along the bending edge and curving of bending edge, as illustrated in Fig. 1, affects geometric accuracy directly. Magee, et al., (1997a) showed that the extent of edge effects depends on the thermal diffusion from the laser beam into the entire plate, and the geometrical constraint of the workpiece as it varies with distance from the end point of the scanning path. The actual profile of bending angle is dependent on the laser processing parameters employed, as well as the material properties. Materials with very different thermal conductivity and expansion exhibited different variation patterns of the bending angle. Attempts have been made to reduce the edge effects by empirically varying the traveling velocity along the scanning path. Results showed that the varying velocity profile could lead to a sizable reduction of the edge effects. Theoretical analysis by Mucha, et al. (1997) showed that thickness in the bending edge region increases due to thermal contraction under the TGM, and the bending edge of the plate is visibly curved due to thermal contraction in the scanning direction. Again, this analytical model does not describe the transient stage, while understanding of the transient stage is useful in analyzing the causes of the edge effects and realizing process control. Numerical and experimental attempts have been made by Bao and Yao (1999) to study the edge effects in more detail.

The energy input and coupling in the laser forming play an important role. They directly affect the deformation process, the resultant geometric shapes, and properties of formed

parts. An approach to describe the input energy is to use the term of "line energy". The line energy, *LE*, of laser scanning is defined as *LE=P/v*, where *P* is the laser power and *v* is the scanning velocity. It is obvious that the line energy represents the energy input per unit length along the scanning path. For processes with the same *LE* but different power/velocity combinations, however, results could vary. Some results by Magee, et al. (1997b) showed the dependence of bend angle on velocity for the α-β *Ti* alloy scanned under the condition of constant line energy. The bend angle first increases with velocity and then levels off. Li and Yao (1999b) studied the issue of *LE* numerically and experimentally, including its effects on dimension, hardness and microstructure.

As known, the strain rate influences the material flow stress, especially at elevated temperatures. The influence on the flow stress translates to that on the forming process and properties of the formed parts, including dimension, residual stresses and hardness of the formed parts. Strain rate effects in laser forming are studied under the condition of "constant peak temperature," that is, the combinations of laser power and scanning velocity are so determined that the peak temperature reached at the top surface of the laser scanned workpiece remains constant (Li and Yao, 1999a). In this way, the constant net energy input available for the forming purpose can be maintained under different scanning velocity (strain rate).

This paper summarizes recent research in laser forming at Columbia University. Materials are presented along the lines of dimensional characteristics and mechanical properties of formed parts to obtain new perspectives. Numerical modeling is first

summarized. Extensive experiments including that under conditions of constant line energy and constant peak temperature are explained. Simulation results are compared with their experimental counterparts, accompanied by detailed discussions.

2. Numerical Simulation

Th basic equations used in numerical simulation are as follows. The basic equation of energy balance is

$$\int_V \rho \dot{U}\, dV = \int_S q\, dS + \int_V r\, dV \tag{1}$$

where V is the volume of a solid material with the surface area S, ρ the density of the material, $\dot{U}$ the material time rate of the internal energy, q the heat flux per unit area of the body flowing into the body, and r the heat supplied externally into the body per unit volume. By neglecting the coupling between mechanical and thermal problems (heat generated by deformation in laser forming is negligible), internal energy U is related to temperature θ by specific heat c:

$$c(\theta) = \frac{dU}{d\theta} \tag{2}$$

where c is the specific heat, θ the temperature of the material, U the internal energy of the material, which is dependent on the temperature only. Heat conduction is assumed to be governed by the Fourier law, i.e., heat flux is proportional to the temperature gradient, with thermal conductivity as the proportional constant. The thermal strain ε^{th} is related to a temperature matrix $\mathbf{T}$ by a linear coefficient of thermal expansion α. The energy balance model for deformation process follows:

$$\frac{d}{dt}\int_V \left(\rho\,\mathbf{v}\cdot\mathbf{v}/2+\rho U\right)dV = \int_S \mathbf{v}\cdot\mathbf{t}\,dS + \int_V \mathbf{f}\cdot\mathbf{v}\,dV \tag{3}$$

where ρ is the current density, $\mathbf{v}$ the speed field vector, U the internal energy per unit mass, $\mathbf{t}$ the surface traction vector, $\mathbf{f}$ the body force vector, $\mathbf{n}$ the normal of boundary S, V the volume in study, and S the corresponding boundary surface.

For isotropic linear elastic metallic materials, the stress, $d\sigma$, can be expressed as:

$$d\sigma = Kd\varepsilon_{kk}\delta_{ij} + 2Gde_{ij} \tag{4}$$

where K is the bulk modulus and G the shear modulus, which can be computed readily from Young's modulus E and Poisson's ratio ν. Both Young's modulus E and Poisson's ratio ν are temperature dependent, and so are bulk modulus K and shear modulus G. Von Mises criterion is used as the yield criterion in the simulation, which is a pressure-independent yield criterion. It takes the following form:

$$\frac{1}{6}\left[(\sigma_1-\sigma_2)^2 + (\sigma_2-\sigma_3)^2 + (\sigma_3-\sigma_1)^2\right] = K^2 \tag{5}$$

where σ_1, σ_2 and σ_3 are principal stresses. K is determined by a uniaxial experiment:

$$\frac{1}{3}\sigma_y^2 = K^2 \tag{6}$$

where σ_y is the yield stress in the uniaxial tension experiment. For plastic deformation, the governing rule is the flow rule, which is given by:

$$d\boldsymbol{\varepsilon} = d\lambda\frac{\partial f}{\partial\boldsymbol{\sigma}} \tag{7}$$

where f is a function of $\boldsymbol{\sigma}$ that describes the yield criterion. With the Von Mises criterion, equation (7) becomes:

$$d\varepsilon_i = \frac{d\bar{\varepsilon}}{d\bar{\sigma}}\left[\frac{3}{2}\sigma_i - \frac{1}{2}\sigma_{kk}\right] \tag{8}$$

where $\bar{\varepsilon}$ is equivalent strain, $\bar{\sigma}$ is equivalent stress. Strain hardening describes the increasing of yield stress with the accumulation of plastic deformation. In laser forming process, though every point of the workpiece experiences a thermal cycle, the mechanical loading, however, as far as the plastic deformation is concerned, is essentially monotonic. Thus, the isotropic hardening rule is adopted. With work hardening, the flow stress is related to strain by:

$$\sigma = K \cdot \varepsilon^n \tag{9}$$

where n is the strain-hardening exponent, and can be found in literature, and K a constant. Strain-rate dependency of material properties is also taken into consideration by assuming that the flow stress is related with strain rate by the following equation:

$$\sigma = D \cdot \dot{\varepsilon}^m \tag{10}$$

where m is the strain rate exponent determined empirically (Li and Yao, 1999a), and D a constant. For convenience, a ratio of real yield stress to static yield stress, $R(\theta,\dot{\varepsilon})$, as a function of temperature θ and strain rate $\dot{\varepsilon}$, is defined as:

$$R(\theta,\dot{\varepsilon}) = \bar{\sigma}\Big/\sigma^0 \tag{11}$$

where $\bar{\sigma}$ is yield stress after considering strain rate, and σ^0 the static yield stress.

By standard Galerkin approach, equation (1) can be discretized in space:

$$\int_V N^N \rho \dot{U}\, dV + \int_V \frac{\partial N^N}{\partial \mathbf{x}} \cdot \mathbf{k} \cdot \frac{\partial \theta}{\partial \mathbf{x}}\, dV = \int_V N^N r\, dV + \int_{S_q} N^N q\, dS \tag{12}$$

where N is the nodal number. This set of equations is the "continuous time description" of the geometric approximation. With the backward difference algorithm

$$\dot{U}_{t+\Delta t} = \frac{U_{t+\Delta t} - U_t}{\Delta t}, \tag{13}$$

equation (12) can be discretized in time domain:

$$\frac{1}{\Delta t}\int_V N^N \rho\left(U_{t+\Delta t} - U_t\right)dV + \int_V \frac{\partial N^N}{\partial \mathbf{x}} \cdot \mathbf{k} \cdot \frac{\partial \theta}{\partial \mathbf{x}} dV - \int_V N^N r \, dV - \int_{S_q} N^N q \, dS = 0 \tag{14}$$

This nonlinear system is then solved by a Modified Newton method.

The following assumptions are made for the numerical modeling. The power density distribution of the laser beam follows a Gaussian function. The laser operates in CW mode. No cooling gas or water jet is employed. Temperature dependency of material properties is considered, including thermal conductivity, specific heat, Young's modulus, Poisson ratio, and flow stress. Elastic strains are assumed much smaller than unity. The rate of deformation is the total strain rate, i.e., the sum of the elastic strain rate and plastic strain rate. Strain hardening of the material is considered through the strain-hardening exponent, which is also temperature dependent. Dependency of flow stress on strain rate is modeled by defining a stress ratio $R(\theta, \dot{\varepsilon})$. Dissipation of energy due to plastic deformation is negligible compared with the intensive laser energy involved. It is assumed that no melting takes place in the forming process.

The boundary conditions are as follows. Laser beam is given as prescribed nonuniform surface heat flux: $q = q(x, y, t)$ on the top surface. On five of the six surfaces (except for the symmetry plane), free convection with air is considered: $q = h\,(\theta - \theta_0)$, where h is the

heat transfer coefficient, and $\theta_0 = \theta_0\,(x, t)$ the surrounding temperature. Radiation is also considered on these five surfaces: $q = A\,((\theta - \theta_Z)^4 - (\theta_0 - \theta_Z)^4)$, where A is the radiation constant, and θ_Z the absolute zero on the temperature scale used. The symmetric plane is assumed adiabatic. Two adjacent points in the middle and bottom of the symmetric plane are fixed in order to remove the rigid body motion. All other points within the symmetric plane are assumed to move only within the symmetric plane throughout the deformation process.

The finite element numerical analysis was carried out using a commercial code ABAQUS. For thermal and structural analysis, the same mesh model is used. In order to simulate the shear process in the laser forming, a three-dimension element with twenty nodes was used because this type of element has no shear locking and hourglass stiffness and is also compatible with thermal stress analysis. A user-defined FORTRAN program was used to model the heat source input from the Gaussian laser beam.

3. Experiment

Laser forming experiments were carried out with a PRC1500 CO_2 laser system with the maximum power of 1.5 kW. The distribution of the power density is Gaussian (TEM_{00}). The diameter of the laser beam is defined as the diameter at which the power density becomes $1/e^2$ of the maximum power value. The samples were made of low carbon steel AISI 1010. The samples were first cleaned using propanol and then coated with graphite coating to obtain relatively known and increased coupling of laser power. The geometry of the samples was measured before and after laser forming using a coordinate measuring

machine. The residual stress was measured using X-ray diffractometry. Samples

obtained from the formed sheet for microstructure observation were mounted, polished,

and etched using a etchant of 3% HNO$_3$ for 20 seconds. The samples were observed

under a scanning electron microscope.

The experimental parameters to investigate the effects of process parameters on average

bend angle are listed in Table 1. Table 2 shows conditions of the experiment for edge

effect study. Under conditions 1 to 3, the bucking mechanism (BM) is likely to dominate

because of the larger beam diameter to sheet thickness ratio. Under condition 5, the

temperature gradient mechanism (TGM) is more likely to dominate because of the

smaller beam-diameter to thickness ratio.

As discussed early, in order to study the strain rate effects in an isolated manner, it is

desirable to create conditions under which strain rate may vary but net energy input

available for the forming purpose remains constant. To approximate the scenario, a

constant peak temperature method was devised. In determining the process parameters

for the condition of constant peak temperature, the scanning velocities are specified first

and the laser powers were iteratively determined using the numerical simulation to give

approximately the same peak temperature at the top surface of the workpiece. Listed in

Table 3 are values determined for a targeted peak temperature of 1,030ºC.

Table 1 The experimental parameters for the investigation of

average bend angle

d L.E.	2mm	3mm	4mm
5 J/mm	V=10-290 mm/s P=50-1450 W	V=10-270 mm/s P=50-1350 W	V=10-280 mm/s P=50-1400 W
7.5J/mm		V=53.3-180 mm/s P=400-1350 W	
10 J/mm			V=40-138 mm/s P=400-1380 W
15 J/mm			V=13.3-90 mm/s P=200-1350 W
20 J/mm			V=2.5-67.5 mm/s P=50-1350 W

(L.E. = Line Energy, P = Power, V = Velocity, d = Beam Diameter

Sample dimension: 80×40×0.89mm)

Table 2 Experimental conditions for edge effect investigations

No.	L.E. (J/mm)	P (W)	V (mm/s)	Size (mm^3)	d (mm)
Condition 1	20	200 – 1300	10 – 67.5	80 x 80 x 0.60	8
Condition 2	20	200 – 1300	10 – 67.5	80 x 80 x 0.89	8
Condition 3	30	200 – 1300	10 – 45	80 x 80 x 0.89	8
Condition 4	30	400 – 1000	13.3 – 33.3	80 x 76.3 x 1.5	8
Condition 5	20	800 – 1300	40 – 65	80 x 76.3 x 2.3	4

Table 3 Experimental and simulation condition under constant peak temperature

Velocity (mm/s)	80	90	100	110	120	140	170
Power (W)	800	843	886	929	970	1040	1130

(beam diameter: 4mm, sample dimension: 80×40×0.89mm)

Please note that for a specific combination of velocity and power, the peak temperature remains approximately constant throughout the scanning path except at both ends of the path (Bao and Yao, 1999). Therefore, the targeted peak temperature refers to the peak temperature throughout the path while ignoring the temperature change at both ends of the path.

4. Results and discussion

4.1. Dimensional characteristics

The dimensional characteristics investigated include average bend angle, bend angle variation, curving of the bending edge, and elongation or contraction in particular directions.

4.1.1. Average bend angle

Shown in Fig. 2(a) is the dependence of average bend angle on scanning speed for different beam diameters but same line energy. It is seen that at lower velocities, the bend angle is smaller despite the line energy is kept constant. This is because that, when the scanning velocity is lower, through-thickness temperature gradient is smaller (Fig. 3).

This, in turn, makes the difference between the thermally induced distortions at the top and bottom surfaces smaller. More importantly, heat dissipation is more significant at lower speeds and that makes the temperature and efficiency of the forming process lower. It can also be seen from Fig. 2(a) that when diameter of the laser beam decreases, the slope of a curve decreases at the higher velocity region, and that in the case of 2mm diameter it even become negative. This is because the material flow stress increases due to increased strain rate caused by higher scanning velocity, and the stress increment due to strain rate variation is more significant at a higher temperature caused by the smaller beam size and/or higher velocity (Li and Yao, 1999b).

Fig. 2(b) shows the relationship between bend angle and scanning speed for the samples scanned at different line energy of 10, 15, and 20 mm/s but with the same beam diameter of 4mm. Obviously, the higher the line energy, the larger the bend angle. When the line energy is higher, the slope of a curve decrease a bit more because higher line energy corresponds to higher temperature that enhances the influence of strain rate on material flow stress.

Shown in Fig. 4 is the simulation and experimental results of the bend angle vs. velocity for the constant-peak-temperature case whose temperature history is presented in Fig. 5. As mentioned earlier, the constant-peak-temperature condition largely separates the effects of strain rate on flow stress from that of temperature. As seen from Fig. 6(a), as the scanning velocity increases, the compressive plastic deformation at top surface becomes smaller. This is obviously due to the increase in strain rate associated with the

increased velocity (Fig. 6(b)). The increased strain rate in turn causes the increase in

flow stress, which makes bending difficult at the increased velocity. Please note that

under the constant-peak-temperature condition, the results in Fig. 6(a) primarily represent

the effect of strain rate on flow stress because the effect of temperature on flow stress can

be neglected. Comparing Figs. 4 and 6(b), it can be seen that the bend angle decreases

about 30% for the nearly doubled strain rate.

4.1.2 Bending angle variation and bending edge curving

Fig. 7 shows a typical thermal-mechanical simulation result where temperature

distribution is superposed on deformation (magnified for easier visualization). Due to

symmetry only half plate is simulated. As seen, it takes about three seconds to scan the

80-mm path at the velocity used, while deformation does not complete till much later. A

curved bending edge is seen at 1,000 seconds. Fig. 8 (a) shows both experimental and

simulation results of the bending angle along the scanning path and they agree each other

quite well. It can be seen that, from the entering end of the scanning path (X = 0), the

bending angle either drops a little and then increases or directly increases towards the

exiting end, where the maximum value occurs. Shown in Fig. 8 (b) is the curvature of the

bending edge vs. velocity. Fig. 8 (c) and (d) show experimental and numerical results of

bending angle variation and relative bending angle variation, respectively. The bending

angle variation is defined as the difference between the maximal and minimal bending

angle along the bending edge for a given condition. The relative bending angle variation

is the ratio of the bending angle variation to the average bending angle.

As mentioned earlier, bending angle variation and bending edge curving (Fig. 8) are termed as edge effects. The causes of the edge effects are described as follows. The peak temperature that points on the top surface along the scanning path experience is shown in Fig. 9. Apparently, the much higher peak temperature at the exiting end is attributed to the reduced heat dissipation near the exit boundary. The fact that the temperature at the exit point is much higher than that at the entrance point (Fig. 9) explains why the bending angle at the exit point differs from that at the entrance point (Fig. 8(a)). This is one reason why the bending angle is not uniform along the scanning direction. The other cause for the bending angle variation is the curved bending edge (Fig. 8 (b)), which will be explained below.

The bending angle variation (Fig. 8 (c)) rises quickly first, peaks at about 20 mm/s, and then levels off or slightly decreases with the increase of velocity. The curvature of the bending edge also starts to decrease in slope significantly at around 20 mm/s (Fig. 8 (b)). It therefore seems reasonable to conclude that the curved bending edge is another reason for the bending angle variation to occur along the scanning direction.

The cause of the curved bending edge is in turn due to the difference in the X-axis contraction between the top and bottom surfaces (Fig. 10). Fig. 10 (a) shows the simulation result of contractions in the X direction on the top and bottom surfaces along the scanning direction. Fig. 10 (b) shows the difference of the two contractions. The simulation result of the bending edge curvature in Fig. 8 (b) is also superposed here for the convenience of discussion. To further explain the X-axis contraction and the reason

for the difference, the time history of plastic strains at a typical location on the scanning

path (X = 20 mm) is examined in Fig. 11. Fig. 11 (a) shows the time history of the

plastic strain on the top surface of that location (in three perpendicular directions). Fig.

11 (b) shows the time history of the X-axis plastic strain on the top and bottom surfaces

at the same location. Near the top layer along the scanning path, compressive strain

occurs in the X and Y directions and tensile strain in Z direction (Fig. 11 (a)). Please

note the sum of these plastic strains is zero at any given time based on the constancy of

volume in plasticity (Mielnik, 1991):

$$d\varepsilon_1 + d\varepsilon_2 + d\varepsilon_3 = 0 \qquad (15)$$

where ε_1, ε_2 and ε_3 are strains in three mutually perpendicular directions. During the

rapid heating stage (at around one second seen in Fig. 11), a significant Y-axis

compressive plastic strain occurs due to the great geometric constraint of the workpiece

in that direction while the tensile plastic strain in the Z direction occurs freely due to the

much less constraint in the thickness direction. Less well known is the compressive

plastic strain in the X direction, which is also caused by the geometric constraint of the

plate in that direction although the constraint is not as great as that in the Y direction.

The bottom surface along the scanning path undergoes a very similar plastic deformation

process as the top surface, except the magnitude is smaller. This is understandable

because under the given experimental condition (condition 3 in Table 2), the buckling

mechanism is dominant and thus the temperature difference between the top and bottom

surface is moderate. A comparison between the plastic strains at the top and bottom

surfaces is shown in Fig. 11 (b). Fig. 11(b) also shows that, during the cooling stage

(after about one-second seen in Fig. 11), the reverse of the X-axis compressive plastic

strain at the top surface is more than that at the bottom surface. This is because, during the cooling stage, the top surface undergoes more Y-axis compressive plastic strain (Fig. 11 (a)) than that at the bottom surface. Based on the constancy of volume, the X-axis compressive plastic strain at the top surface reverses more than that at the bottom surface (Fig. 11 (b)). Therefore, the total X-axis contraction near the bottom layer is larger than that near the top layer (Fig. 10). Consequently, the bending edge is curved away from the laser beam (Figs. 1 and 7).

As seen in Fig. 10 (b), the greater is the difference between the contractions near the top and bottom surfaces, the greater the curvature. The fact that the curvature increases with velocity can be explained by the increase in average bending angle with velocity. Obviously, when the average bending angle is larger, the above-mentioned difference between the top and bottom surfaces will be more pronounced, and therefore the curvature will be greater.

So far, our discussion has been focused on condition 3 in Table 2 where the buckling mechanism (BM) of laser forming dominates. Under the condition, the edge effects are characterized by a concave bending angle variation (Fig. 8(a)) and the scanning edge is curved away from the laser. Similar results are obtained in experiments and simulation under conditions 1 and 2. Under conditions 4 and 5, however, the BM may not dominate. In fact, under condition 5, the temperature gradient mechanism (TGM) dominates due to the reduced beam diameter and increased plate thickness. Condition 4 represents the situation where the BM transits to the TGM or the BM and TGM co-exist. Therefore, the

edge effects exhibit patterns different from condition 3. As seen from Fig. 12 (a), the

bending angle variation measured along the scanning path is almost linear under

condition 4. Experimental and simulation results show the bending angle variation is

convex under condition 5 (Fig. 12 (b)). In addition, the scanning edge is curved towards

the laser under condition 5 as opposed to curving away from the laser under condition 3.

The time history of the X-axis contraction for conditions 3 and 5 is plotted in Fig. 13. As

seen from Fig. 13 (a), the top and bottom layers experience similar contraction during the

heating stage for the BM-dominated bending operation (condition 3) where temperature

difference between the top and bottom surfaces is moderate. But the bottom layer

contracts more than the top layer during the cooling stage because the Y-axis contraction

at the top surface is greater than that near the bottom surface. This leads to a bending

edge curved away from the laser. For the TGM-dominated bending operation where the

temperature difference between the top and bottom layers is much greater (condition 5),

the top layer contracts more than the bottom layer during the cooling stage (Fig. 13 (b))

simply because the temperature gradient in the thickness direction is so dominant that it

overwrites other effects.

4.2 Mechanical properties
4.2.1 Residual stresses

Fig. 14 shows the numerical simulation and experimental results for the Y-axis residual

stress on the top surface of the workpiece formed under the condition of constant peak

temperature (Table 3). The trends, namely, the bend angle decreasing and residual stress

increasing with the increase of scanning velocity (strain rate) are consistent with the understanding of the forming mechanisms. Fig. 15 plots the time history of temperature, Y-axis plastic strain, and Y-axis stress for low and high strain rate cases (V=80mm/s, P=800W, and V=170mm/s, P=1130W). Please note that all quantities in Figs. 14 and 15 are for the top surface on the scanning path where more changes take place during forming than at the bottom surface. As seen in Fig. 15, the temperature profiles are expectedly very similar between the two cases because these cases are determined to have the same peak temperature in the first place. But the strain rate and in turn the flow stress are quite different between the two cases.

It can be seen from the time history of stress that, with the imminent arrival of the laser beam, a small tensile stress first develops due to the expansion of the preceding area, which is being heated by the laser. With the laser beam arrival and temperature rise, material tends to expand but undergoes significant compressive stress due to mechanical constraints of the surrounding material. When temperature rises further, the flow stress decreases and plastic deformation accrues, which releases the compressive stress and the absolute value of the compressive stress starts to reduce. After temperature reaches its maximum value, the material contracts due to the reduced temperature and the stress starts to change towards being tensile. At the same time, the tensile stress continues to rise as the material immediately ahead is being heated up by the laser beam and expands. Since the flow stress associated with the high velocity (strain rate) is higher, the tensile stress due to the thermal expansion of the material immediately ahead also rises higher. As a result, the residual stress corresponding to the high velocity remains higher than that

for the low velocity, although in both cases the stress falls slightly because of the

contraction of the material immediately ahead. The effect of strain rate on residual stress,

however, is relatively moderate. As seen from Figs. 14 and 6(b), when the strain rate is

nearly doubled between the lower and higher speed cases, the residual stress increases by

about 15%.

Shown in Fig. 16 is a typical Y-axis plastic strain, elastic strain and residual stress

distribution at the top, middle and bottom layers along the scanning path. As seen from

Fig. 16, the plastic strain near both ends of the scanning path is small because the reduced

geometric constraint of the plate in these regions, while along the rest of the scanning

path significant compressive plastic strain is seen. This clearly explains why the residual

stress is compressive at both ends and tensile along the rest of the scanning path.

As seen in Fig. 16, the profile of the residual stress distribution is understandably very

similar to that of the elastic strain distribution. The small shift along the vertical axis is

governed by the relationship for isotropic elasticity, that is,

$$E_{22} = \frac{1}{E_Y}\left[T_{22} - v\left(T_{33} + T_{11}\right)\right] \tag{16}$$

where E_{22} is the elastic strain in the Y direction, T_{11}, T_{22} and T_{33} are stress in the X, Y and

Z direction, respectively. In this case, $T_{33} \approx 0$. Shown in Fig. 17 is the contour plot of

the Y-axis residual stress along the scanning path and within the symmetric plane.

4.2.2 Hardness

The hardness of the deformed workpiece is measured at the top surface along the scanning path (Fig. 18). The measurement is taken 6 days after the forming is done. As seen, the hardness decreases with the increase of velocity (shown in brackets), because of the effect of work hardening. At lower velocities, the strain rate and thus flow stress is lower, resulting higher plastic strain. The higher plastic strain leads to more significant work hardening. A simple calculated relationship between the hardness and plastic strain is also superposed on Fig.18 that agrees with the measurement data. The calculation is based on the well known empirical relationship between stress and hardness as well as $\sigma = K' \varepsilon^n$, where ε is the simulated plastic strain, n the work-hardening exponent for low carbon steel, and K' constant. A reasonable agreement is seen.

4.3 Microstructure

The microstructure of the deformed workpiece is examined using scanning electron microscopy. Shown in Fig. 19 is a typical set of SEM micrograghs for the cross section of the scanning path under the condition of V=138 mm/s and P=1380 W. The simulated temperature at the top and bottom surfaces along this scanning path is about 1380 ^{o}C and 420 ^{o}C, respectively, as shown in Fig. 3. Shown in Fig. 19a is the microstructure of the workpiece material, low carbon steel AISI 1010, as received. Large grains of dark ferrite scattered with light-colored carbide particle are seen. Fig. 19b shows an area very close to the top surface where grain recrystallization is evident after laser forming. As mentioned earlier, the top surface undergoes significant plastic deformation at temperature above the recrystallization temperature. Laser forming may impart some beneficial properties to the workpiece top surface under the condition. Some dissolution

of carbides is also seen due to the high temperature. Fig.19c shows the microstructure near the bottom surface. Little change is observed because the region near the bottom surface undergoes much less plastic deformation (Fig. 6(a)) and the peak temperature reached there is also much lower.

5. Conclusions

Numerical and experimental investigations of laser forming processes are carried out to better understand the influence of process parameters on dimensional characteristics and mechanical properties of the formed parts. The research on strain rate effects are also conducted under that condition of constant peak temperature, which largely isolates the effects of strain rate from that of temperature. With strain rate increase, the thermal-induced distortion decreases and bend angle reduces. The bend angle decreases by about 30% for nearly doubled strain rate under the conditions used. Under the condition of the constant line energy, the bend angle increases with scanning velocity and the degree of increase reduces with the velocity. Edge effects are characterized by a concave pattern in the bending angle variation along the scanning path and a bending edge curved away from the laser under BM-dominated conditions. For the TGM-dominated process, the pattern of edge effects is different, which is characterized by a convex bending angle variation and the bending edge curved towards the laser. In the case of the BM-dominated bending operation, the X-axis contraction near the bottom surface is more significant than that near the top surface, resulting a bending edge curved away form the laser, while the opposite is true in the case of the TGM-dominated bending process. Whether to obtain a convex or concave pattern of the bending angle variation is closely

related with the direction of the curved bending edge. For the constant-peak-temperature case, residual stress in the Y direction increases moderately with strain rate. For the doubled strain rate, residual stress increases by about 15% under the conditions used. With the strain rate increase, the hardness of the formed sample decreases due to the reduced work hardening. Recrystallization and dissolution of hard particles occur near the top surface of the workpiece material used where temperature is higher and plastic deformation is more severe.

Acknowledgements

References

Alberti, N., Fratini, L., Micari, F., 1994, "Numerical simulation of the laser bending process by a coupled thermal mechanical analysis," *Laser Assisted Net shape Engineering, Proceedings of the LANE'94*, Vol. 1, Meisenbach Bamberg, pp. 327-336.

Arnet, H., and Vollertsen, F., 1995, "Extending laser bending for the generation of convex shapes," *IMechE Part B: Journal of Engineering Manufacture*, Vol. 209, pp. 433-442.

Bao, J., Yao, Y. L., 1999, "Study of edge effects in laser bending," to be presented at *1999 International Mechanical Engineering Congress and Exposition*, Nashville, TN, 1999.

Holzer, S., Arnet, H., Geiger, M., 1994, "Physical and numerical modeling of the buckling mechanism," *Laser Assisted Net shape Engineering, Proceedings of the LANE'94*, Vol. 1, Meisenbach Bamberg, pp. 379-386.

Hsiao, Y.-C., Maher, W., et al., 1997, "Finite element modeling of laser forming," *Proc. ICALEO'97*, Section A, pp. 31-40.

Li, W., and Yao, Y. L., 1999a, "Numerical and experimental study of strain rate effects in laser forming," submitted *to ASME Trans., J. Manufacturing Science and Engineering*.

Li, W., and Yao, Y. L., 1999b, "Laser forming with constant line energy," in preparation.

Magee, J., Watkins, K. G., Steen, W. M., Calder, N., Sidhu, J. and Kirby, J., 1997a, "Edge effects in laser forming," *Laser Assisted Net shape Engineering 2, Proceedings of the LANE'97*, Meisenbach Bamberg, pp. 399-408.

Magee, J., Watkins, K. G., Steen, W. M., 1997b, "Laser forming of aerospace alloys," *ICALEO '97, Section E*, pp. 156-165.

Magee, J., Watkins, K. G., Steen, W. M., 1998, "Advances in laser forming," *Journal of Laser Application,* Vol. 10, pp. 235-246.

Mielnik, E. M., 1991, Metalworking Science and Engineering, McGraw-Hill, Inc.

Mucha, Z., Hoffman, J., Kalita, W., Mucha, S., 1997, "Laser forming of Thick free plate," *Laser Assisted Net shape Engineering 2, Proceedings of the LANE'97*, Meisenbach Bamberg, pp. 383-392.

Sprenger, A., Vollertsen, F., Steen, W. M., Waltkins, K., 1994, "Influence of Strain Hardening on Laser Bending," *Laser Assisted Net shape Engineering, Proceedings of the LANE'94*, Vol. 1, Meisenbach Bamberg, pp. 361-370.

Vollertsen, F., 1994, "Mechanism and models for laser forming," *Laser Assisted Net Shape Engineering, Proceedings of the LANE'94*, Vol. 1, pp. 345-360.
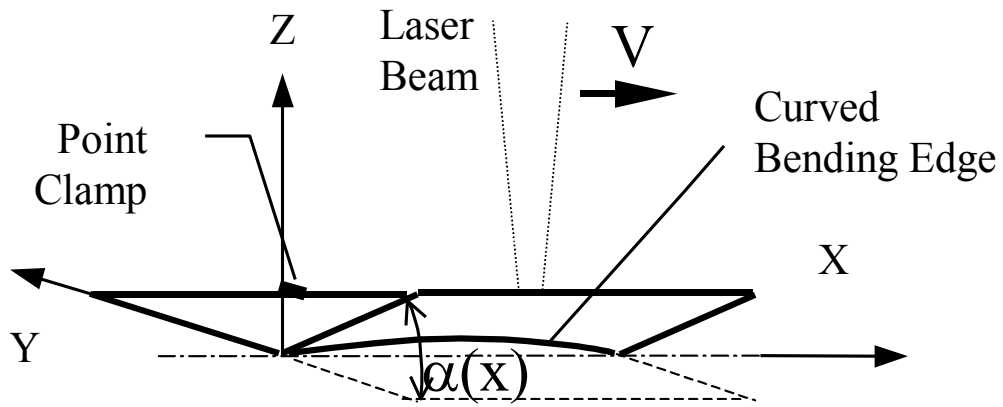
Fig. 1 Schematic of straight-line laser forming showing edge effects characterized by the curved bending edge and non-uniform bending angle varying along the scanning path $\alpha(x)$
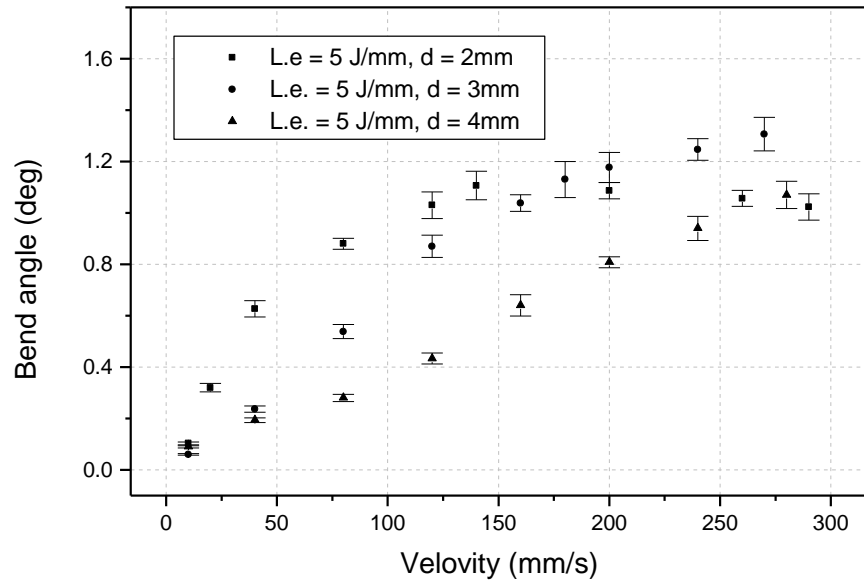
(a)
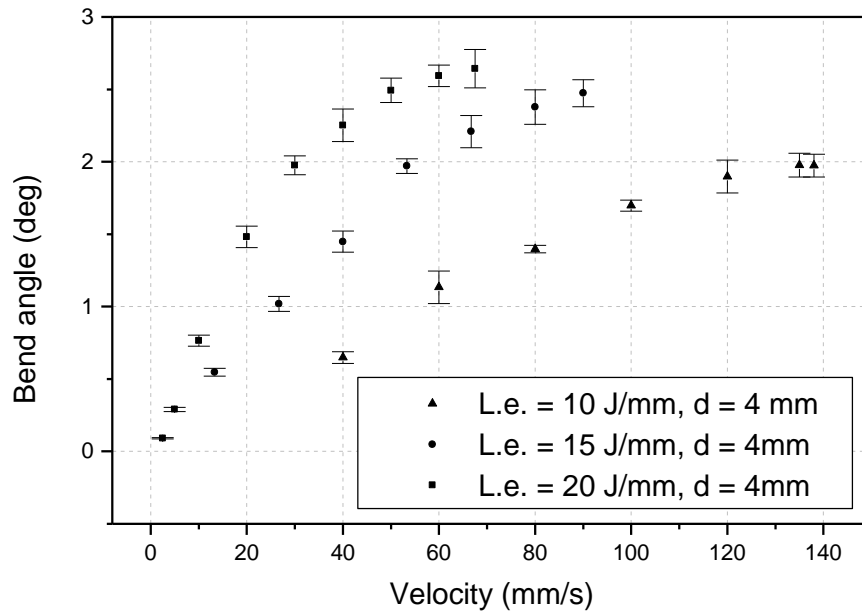
(b)

Fig 2. Bend angle vs. scanning velocity with constant line energy *L.e.* and different beam diameter *d* (a) and with constant beam diameter *d* and different line energy *L.e.*(b) (dimension: 80×40×0.89mm)
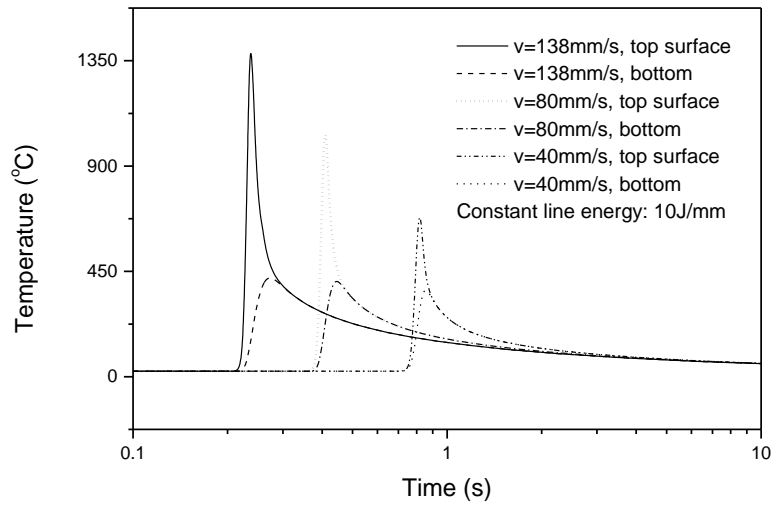
Fig.3 Simulated time histories of temperature under constant line energy (beam diameter: 4mm, dimension: 80×40×0.89mm)
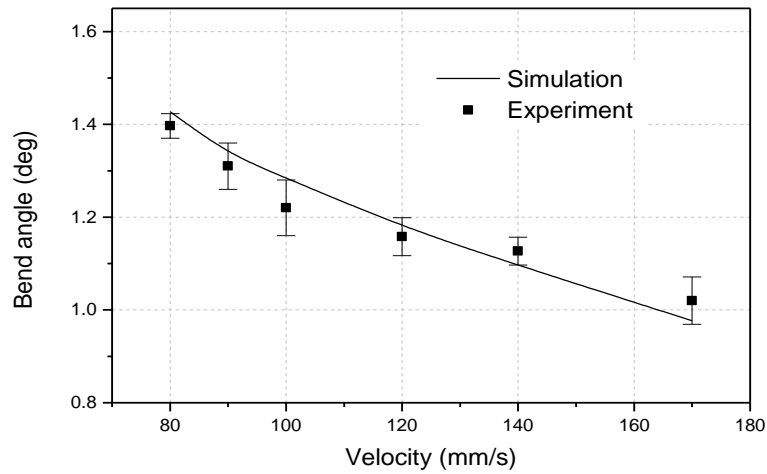
Fig. 4 FEM and experimental results under the condition of constant peak temperature (beam diameter: 4mm, dimension: 80×40×0.89mm)
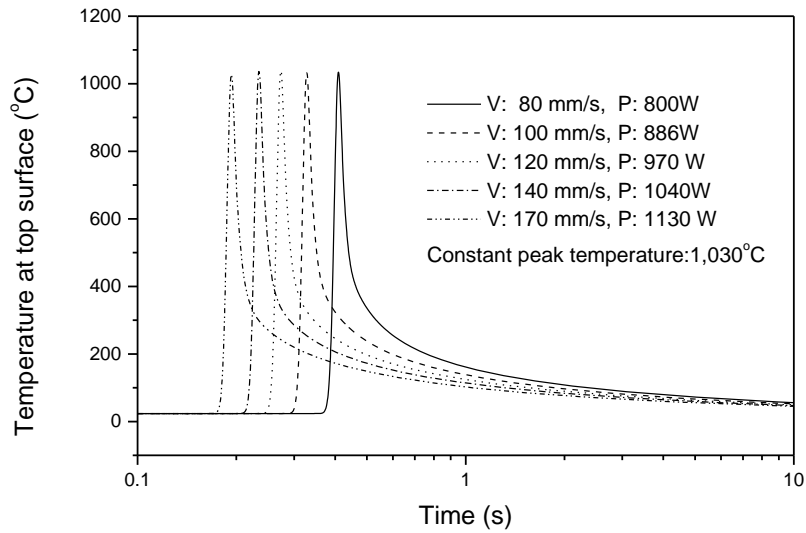
Fig. 5 Simulated time histories of temperature to find different combinations of velocity and laser power that generate approximately the same peak temperature at the top surface (beam diameter: 4mm, dimension: 80×40×0.89mm)
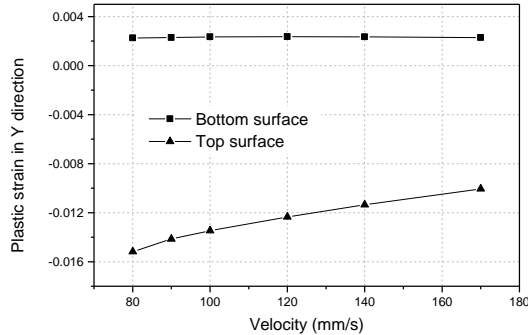
(a) Plastic strain
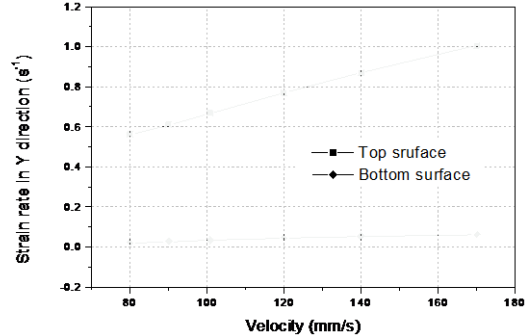
(b) Strain rate

Fig.6 Plastic strain and strain rate in Y direction vs. velocity (constant peak temperature, beam diameter: 4mm, dimension: 80×40×0.89mm)

(a) 1.52 s

(b) 1,000s
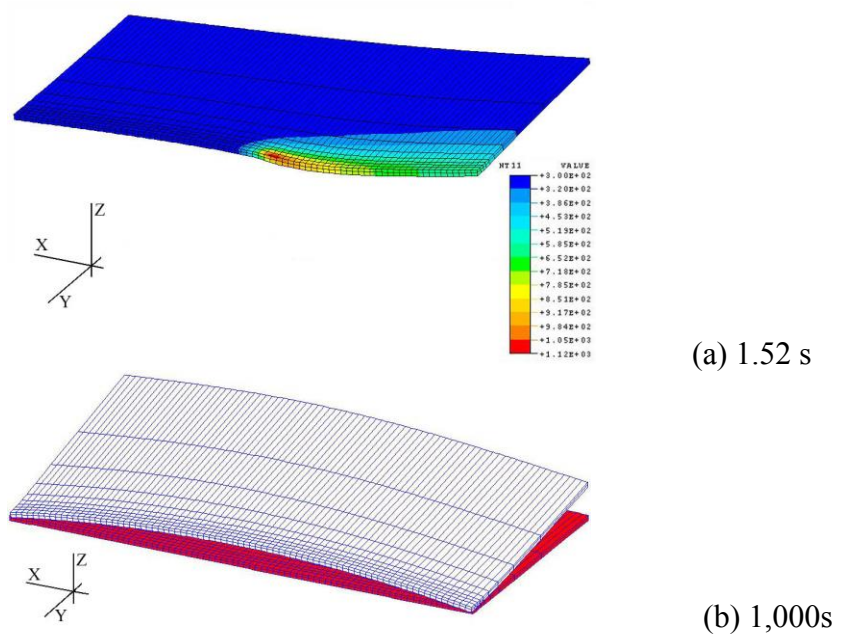
Fig. 7 (a) Temperature distribution in laser bending (deformation magnification 10X), and (b) original and deformed plate (deformation magnification 5X, Half plate, condition 3, V=26.7 mm/s)
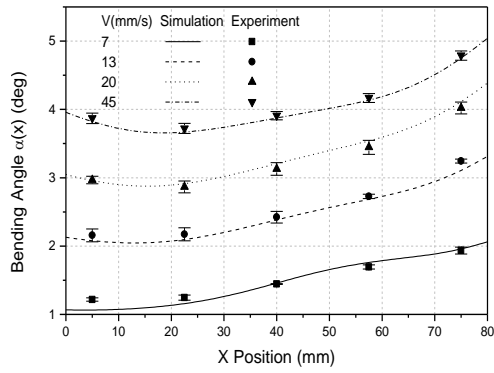
(a)
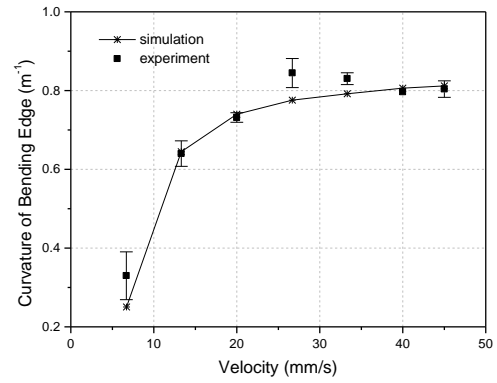
(b)
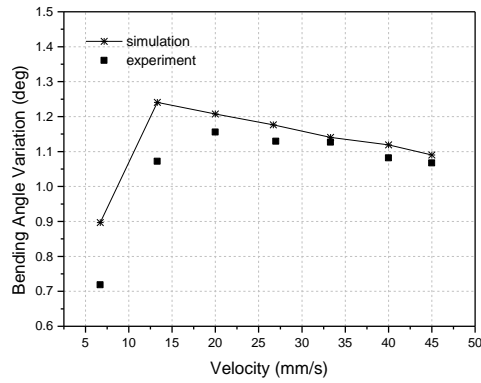
(c)
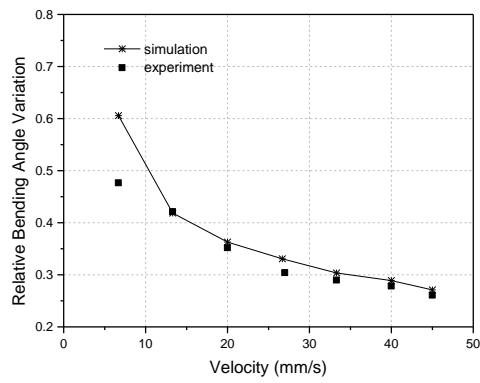
(d)

Fig. 8 Results of simulation and experiment under condition 3 showing edge effects (a) bending angle variation along the scanning path, (b) curvature of the bending edge, (c) bending angle variation (difference between the max and min), and (d) relative bending angle variation (bending angle variation over average bending angle)
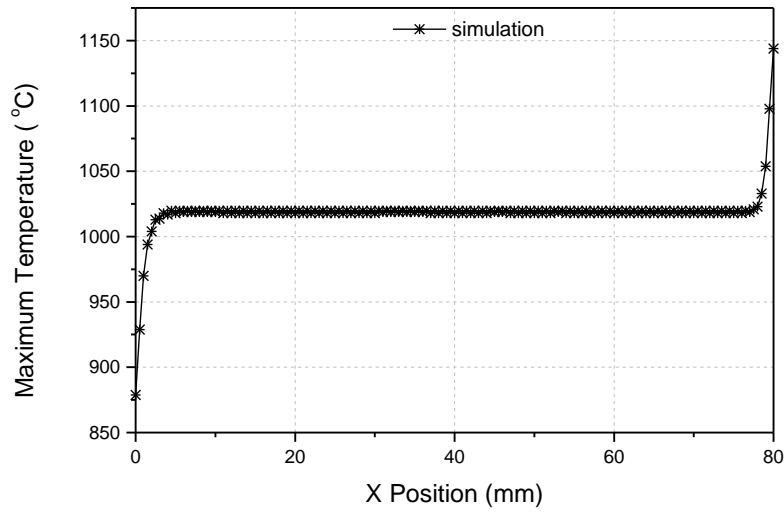
Fig. 9 Typical peak temperature reached on the top surface along the scanning path (Condition 3, V = 45 mm/s)

(a)   (b)
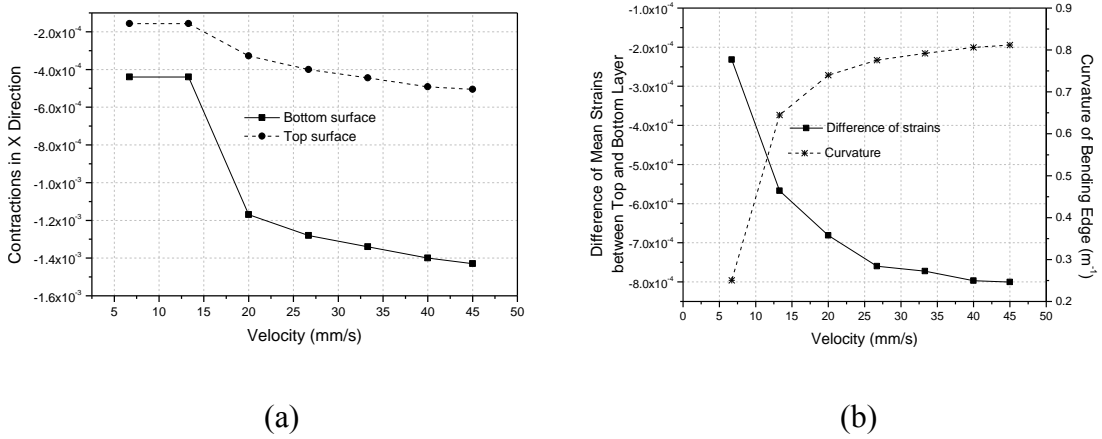
Fig. 10 (a) Contractions in the scanning direction (X-axis), and (b) difference of mean strains between the top and bottom layer along the X-axis and curvature of the bending edge (Condition 3)

(a)   (b)
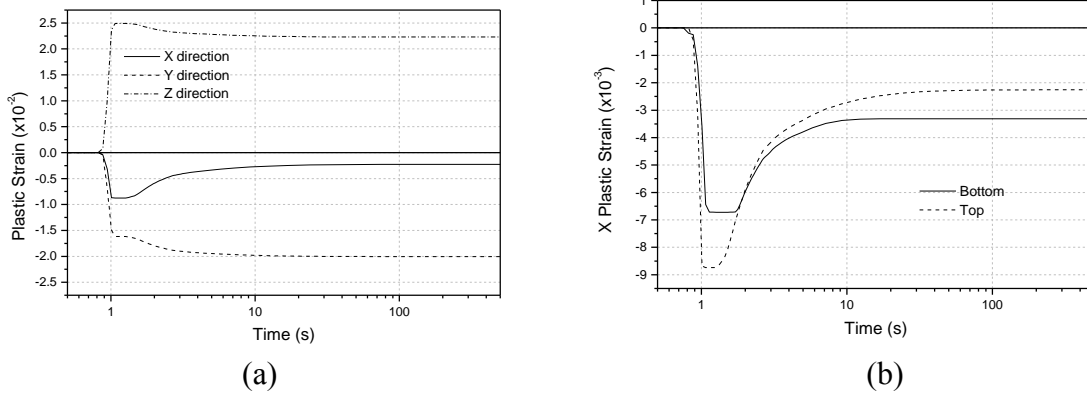
Fig. 11 Time history of plastic strain for a typical point (X = 20 mm) (a) X-, Y-, and Z-axis plastic strain on the top surface along the scanning path, and (b) X-axis plastic strain on the top and bottom surfaces along the scanning path (Condition 3, V = 26.7 mm/s)

(a)   (b)
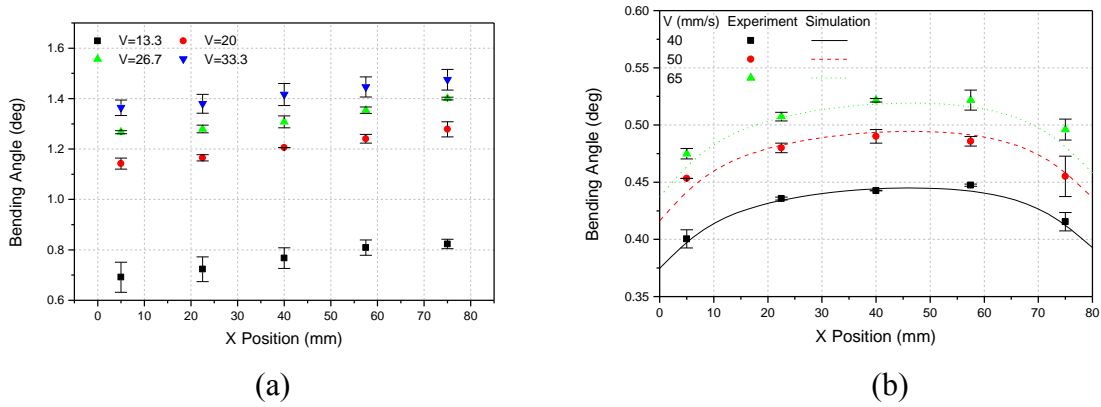
Fig. 12 (a) Measurement of bending angle α(x) (Condition 4), and (b) simulation and experimental results of bending angle α(x) (Condition 5)

(a)   (b)
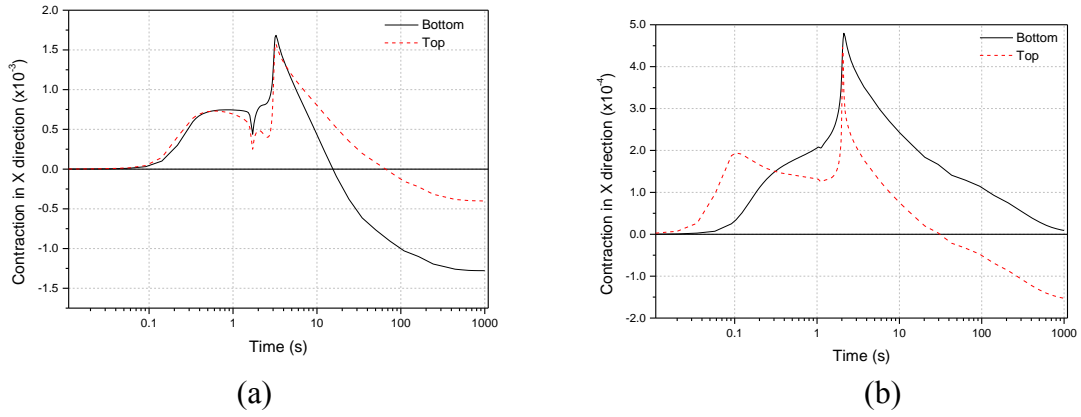
Fig. 13 Time history of X-axis deformation (a) condition 3 (Buckling mechanism dominated), and (b) condition 5 (Temperate gradient mechanism dominated)
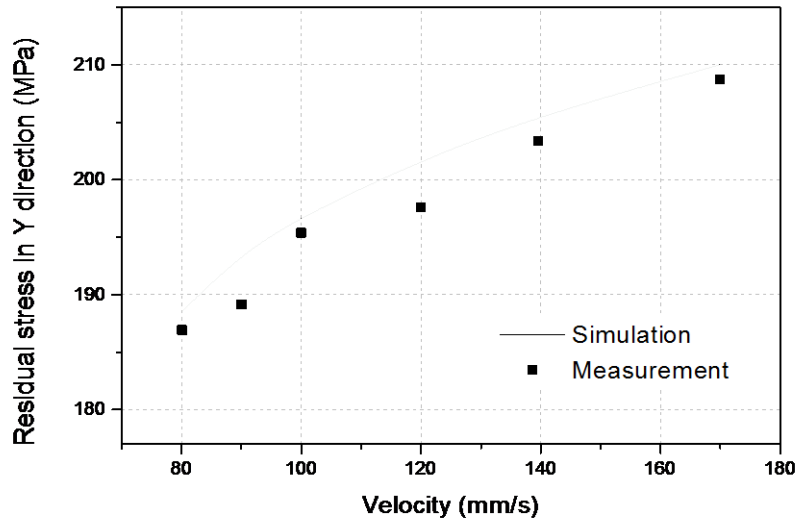
Fig. 14 FEM and X-ray diffraction measurement of residual stress for the samples scanned under the condition of constant peak temperature (beam diameter: 4mm, dimension: 80×40×0.89mm)
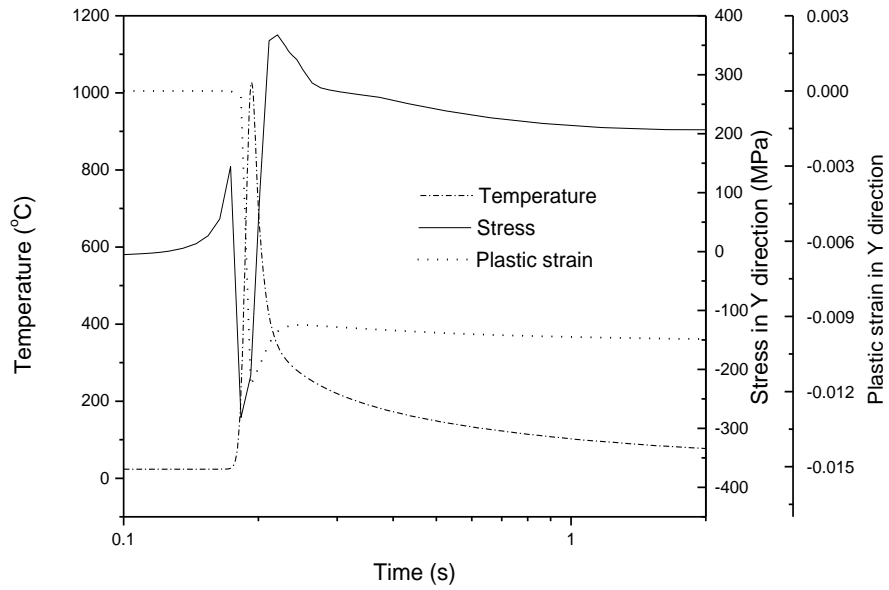
(a) V=170mm/s, P=1130W
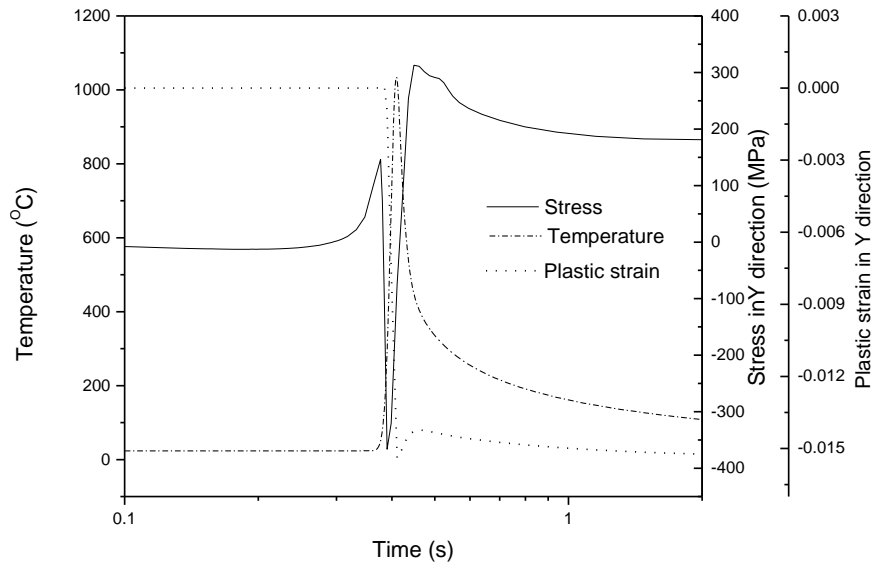
(b) V=80mm/s, P=800W

Fig. 15 Comparison of effect of high and low strain rate on residual stress (beam diameter: 4mm, dimension: 80×40×0.89mm)
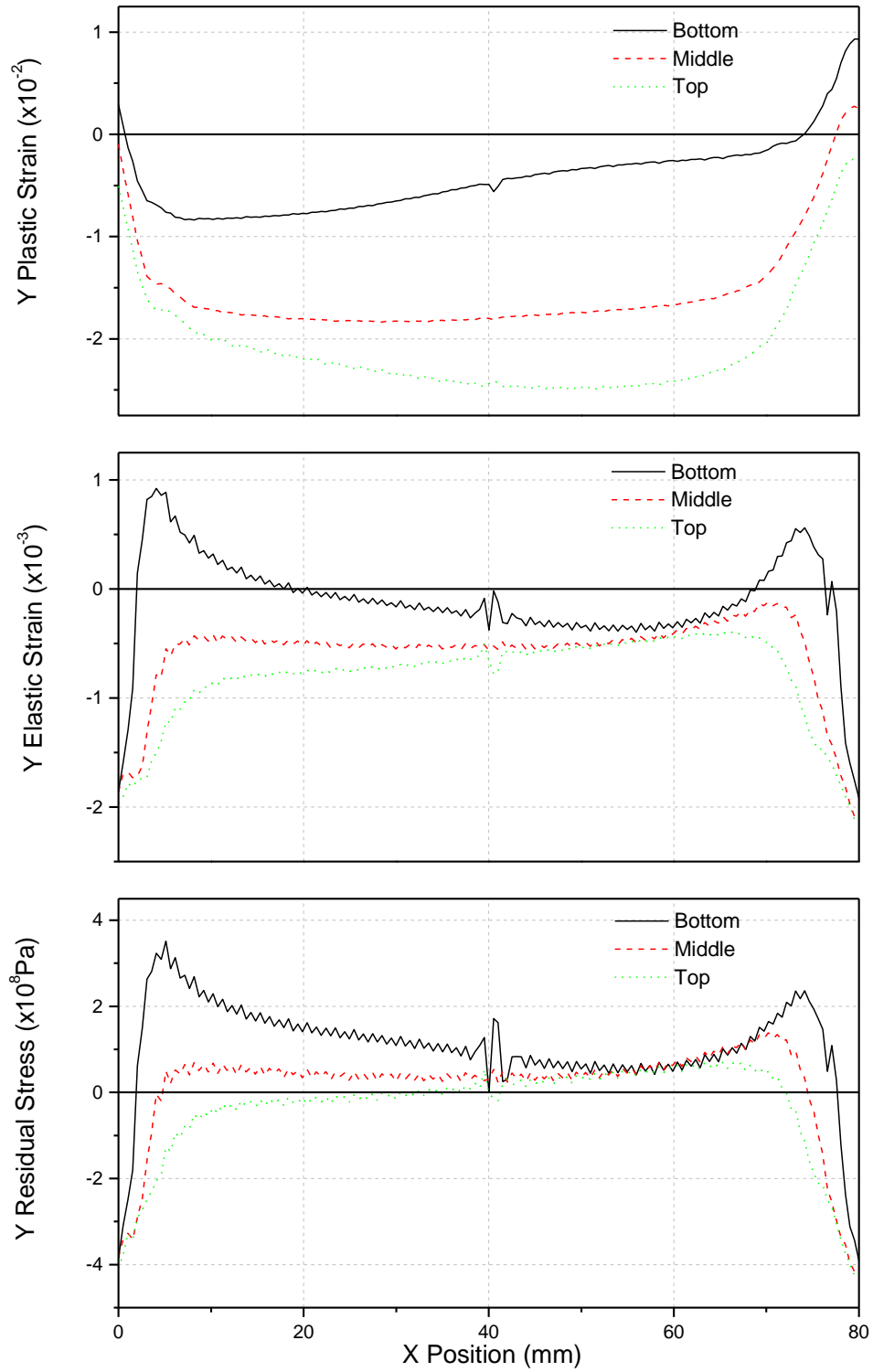
Fig. 16 Y-axis plastic strain, elastic strain and residual stress along the scanning path
(Condition 3, V = 26.7 mm/s)
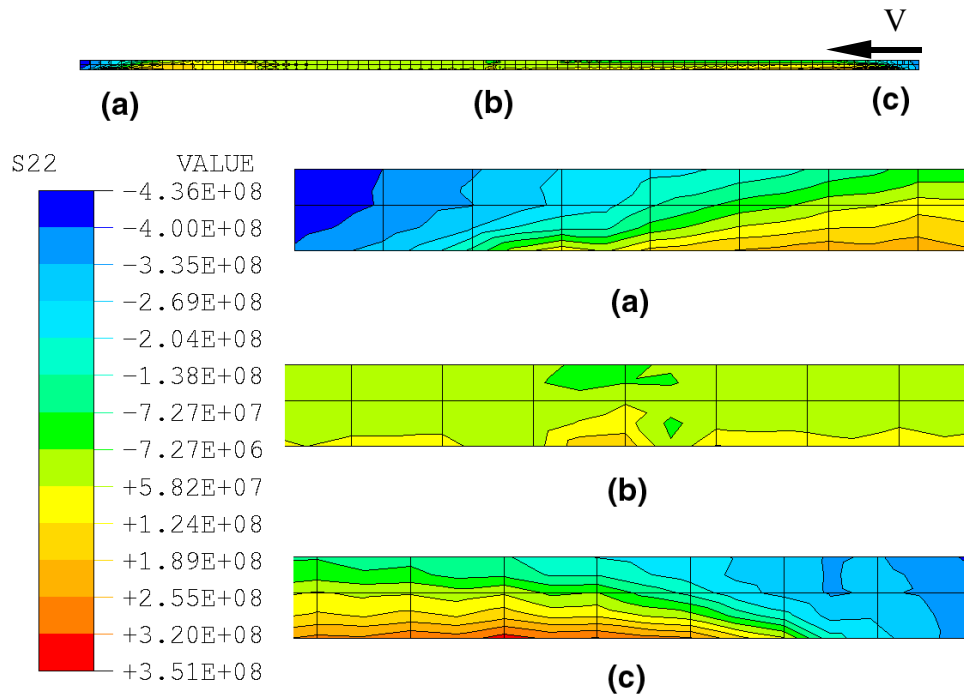
Fig. 17 Contour plot of Y-axis residual stress along the scanning path and within the symmetric plane (Condition 3, V = 26.7 mm/s)
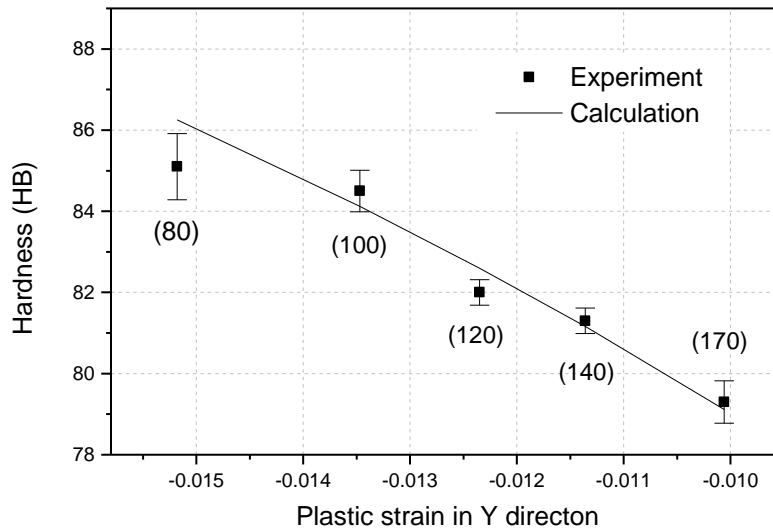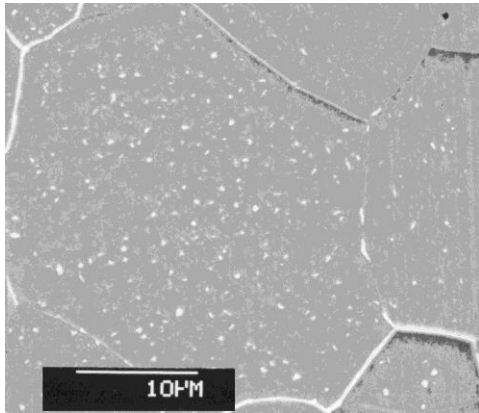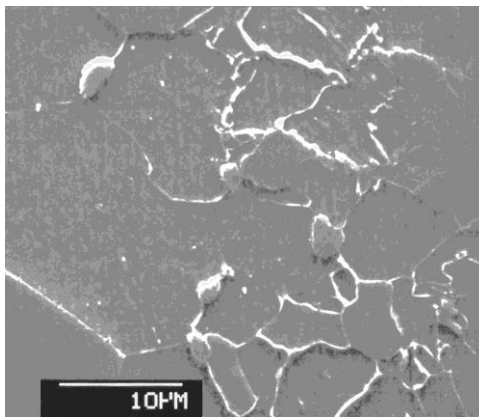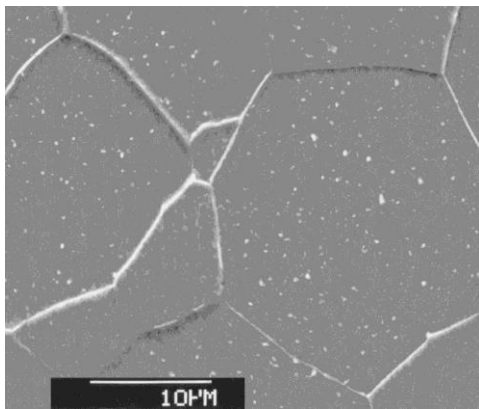

Fig. 18 Hardness vs. simulated plastic strain in Y direction under the condition of constant peak temperature (Data in brackets are the corresponding scanning velocities in mm/s, beam diameter: 4mm, dimension: 80×40×0.89mm)

(a) as received

(b) After laser forming (near top surface)

(c) After laser forming (near bottom surface)

Fig. 19 Scanning electron micrograghs of the microstructure of the scanning path region
(V:138mm/s, P:1380W, AISI1010, beam diameter: 4mm, dimension: 80×40×0.89mm)